Thermomechanical Effects of Intense Thermal Heating on Materials/Structures

C. I. Chang,* C. A. Griffis,† F. R. Stonesifer,‡ and J. A. Nemes†
Naval Research Laboratory, Washington, DC

An analytical methodology for prediction of the response of metallic and composite structures subjected to combined intense heating and applied mechanical loading is presented. The proposed methodology includes a thermal analysis that incorporates nonlinear phenomena such as temperature-dependent thermophysical properties, re-irradiation losses, and ablation/melting phenomena. A detailed description of a sequential, finite-element, ply-by-ply failure analysis based on the maximum stress criterion is given for composite structures as well as a limit analysis approach for metallic structures. Computational projections are substantiated by experimental measurements for an aerospace aluminum alloy and a graphite epoxy plate specimen exposed to simultaneous intense heating and applied tensile loading.

I. Introduction

WHEN composite or metallic structures are subjected to intense rapid heating, their performance is drastically impaired due to thermal degradation of mechanical properties and ablation/melting of critical load-bearing components.[1,2] Additional adverse effects of a severe thermal environment include generation of high thermal stress and the development of substantial stress intensification in regions of localized burnthrough.[3] Over the past several years the Naval Research Laboratory has been engaged in the development of a generalized analytical methodology for prediction of the response of advanced structures simultaneously exposed to intense heating and applied service loads. The objective of this paper is to summarize the key factors in this model and to illustrate its application on simple structural elements. In general, formulation of the methodology requires definition and integration of three major components which include: an elevated-temperature material property data base; an appropriate nonlinear thermal analysis; and a stress/fracture analytical capability.

II. Thermal Modeling

The primary function of the thermal analysis is to define the transient spatial temperature and ablation distributions that are needed as input into the stress and fracture calculations, which in turn determine the overall structural survivability prediction. To illustrate the fundamental aspects of the thermal modeling it is convenient to first consider a one-dimensional problem in which a plate of thickness L is subjected to uniform constant intensity on one surface. The material is assumed to be undergoing ablation on the irradiated surface, with the associated recession rate denoted by V. In the present formulation it is further assumed that ablation occurs when, at the heated surface, a constant temperature T_s is attained and a constant ablation energy H_s is absorbed. For mathematical convenience a convective coordinate z is adopted that moves continuously with the planar ablation front. It is readily shown that for the present problem the Fourier heat conduction equation is given by

$$\frac{\partial}{\partial z}\left[k\frac{\partial T}{\partial z}\right]+\rho C_p V\frac{\partial T}{\partial z}=\rho C_p\frac{\partial T}{\partial t} \tag{1}$$

where $T(z,t)$, k, ρ, and C_p represent temperature, thermal conductivity, density, and heat capacity, respectively. It should be noted that the ablation velocity V is a function of time t. The boundary conditions on the irradiated surface ($z=0$) include

$$T(0,t)=T_s=\text{const} \tag{2}$$

and a straightforward energy balance expressed by

$$\rho H_s V=\alpha I_o+k\frac{\partial T}{\partial z}+I_r+I_{cv} \tag{3}$$

in which I_o represents the incident heat flux, α is the absorptivity, and I_r and I_{cv} denote the re-irradiation and convection heat losses, respectively. At the rear unheated surface, an insulation is frequently adopted, i.e.,

$$\frac{\partial T}{\partial z}=0 \text{ at } z=L-z_b \tag{4}$$

where z_b denotes the depth of the ablation front measured from the original surface position. Griffis et al.[4] contains a finite-difference formulation for Eqs. (1-4) based on a modified Crank-Nicolson method as well as a computational algorithm for their numerical solution.

For two-dimensional, axisymmetric heat transfer problems, a lumped-mass finite-difference model has been developed as indicated in Fig. 1. The basic difference equations are readily derived by considering a generic surface element i subjected to incident, re-irradiation, and convective heat fluxes I_o,I_r, and I_{cv}, respectively. Over a time increment Δt the element also absorbs heat ΔQ_c through conduction from surrounding elements designated 1, 2, and 3

$$\Delta Q_c=\sum_{j=1}^{3}K_{ij}(T_i-T_j) \tag{5}$$

where T_j is the temperature associated with element j, and K_{ij} represents an effective conductivity between the adjacent elements i and j. In general, K_{ij} is a function of the dimensions and conductivities of the two elements in question and Griffis et al.[5] contains explicit mathematical expressions for K_{ij} for

Received Nov. 18, 1985; revision received June 12, 1986. This paper is declared a work of the U.S. Government and is not subject to copyright protection in the United States.

*Branch Head, Structure Integrity Branch.
†Mechanical Engineer, Structure Integrity Branch.
‡Materials Research Engineer, Structure Integrity Branch.

both radial and through-thickness heat flow. The fundamental difference equations are obtained by equating the heat acquired by the element through incident heat, re-irradiation, convection, and conduction to that associated with the specific heat effect ΔQ_{cp}. The latter quantity is given by

$$\Delta Q_{cp} = r_i l_i d_i \rho C_i \Delta T_i \tag{6}$$

in which the volume of the element (subtended angle equal to unity) is $r_i l_i d_i$, and C_i denotes the elemental heat capacity. Applications of the energy balance give

$$\Delta T_i = \left[\sum_{j=1}^{3} K_{ij}(T_j - T_i) + r_i l_i \alpha I_o + r_i l_i \sigma \epsilon (T_o^4 - T_i^4) + r_i l_i h (T_r - T_i) \right] \Delta t \Big/ r_i l_i d_i \rho_i C_i \tag{7}$$

where σ, ϵ, T_o, h, and T_r represent the Stefan-Boltzmann constant, surface emissivity, ambient temperature, convection coefficient, and recovery temperature, respectively. Since all quantities on the right-hand side of Eq. (7) are evaluated at the end of the previous step, the present formulation constitutes an explicit forward difference method wherein the temperature for each element in the mesh is computed at successive time steps to generate the complete transient thermal response of the structure. Equation (7) can easily incorporate temperature-dependent properties and can accommodate ablation phenomenon by introducing a large heat capacity value close to the prescribed ablation temperature. When a given surface element ablates, the incident radiation I_o is transferred to an appropriate adjacent element in the depthwise direction.

In addition to constituting a major factor in structural survivability assessment, both the one- and two-dimensional thermal models discussed above have been extensively employed in conjunction with experimental measurements to establish important thermophysical properties at rapid heating rates. This technique entails experimental determination of the transient temperature response of instrumented test coupons which are exposed to varying degrees of intense heating. The experimental data for various thicknesses of material are then compared with analytically derived temperature vs time results in which assumed temperature-dependent heat capacities and conductivities are utilized. The correct material properties are established by systematic iterative adjustment of the assumed properties until satisfactory agreement is attained between the analytical and experimental results over the entire spectrum of specimen thicknesses and heating intensities. The iterative process can be continued until the desired degree of accuracy is achieved. Figure 2 illustrates the resulting dependence of temperature of conductivity[4,6] and specific heat[6] for AS/3501-6 graphite epoxy.

Figures 3 and 4 illustrate typical comparisons between analytical and experimental thermal responses for laminated AS/3501-6 graphite epoxy coupons having 24 and 96 plies, respectively. To simulate rapid intense heating in a controlled manner, the specimens were spot-irradiated at a peak intensity of 2.9 kW/cm^2 using the 15-kW continuous wave, 10.6-μ(CO_2) laser device at the Naval Research Laboratory. Absorptivities at 10.6 μ for graphite epoxy and coated aluminum are 0.92 and 0.93, respectively.[4,5] Figure 5 describes the stacking sequence, thermocouple location, and specimen geometry employed in the laser experiments. The analytically derived curves shown in Figs. 3 and 4 were obtained using the

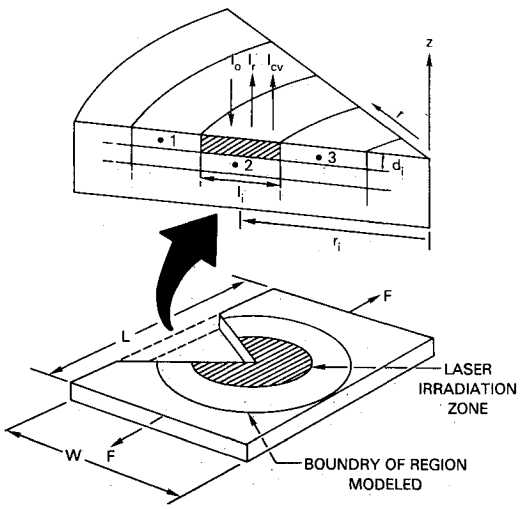

Fig. 1 Geometric description of lumped-mass heat transfer model.

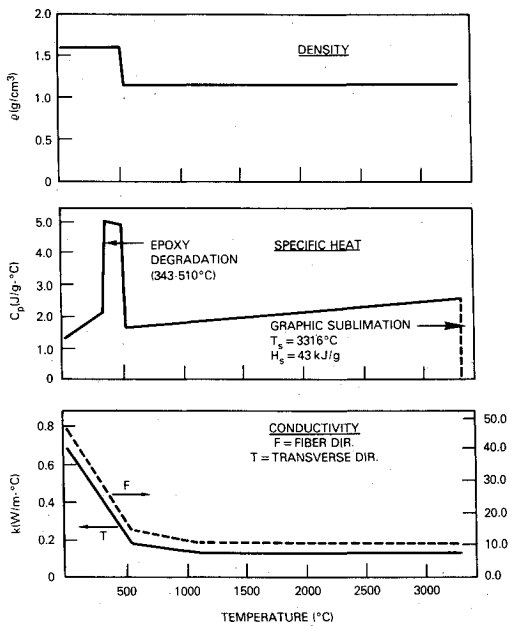

Fig. 2 Temperature dependence of thermophysical properties of AS/3501-6 graphite epoxy.

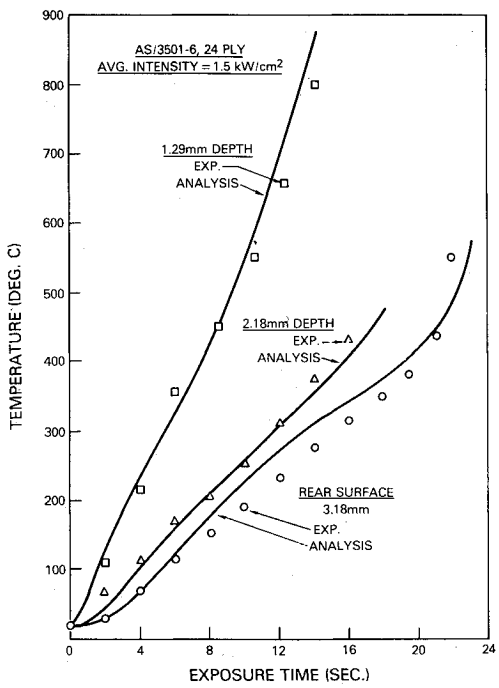

Fig. 3 Comparison of theoretical and experimental thermal response for 24-ply graphite epoxy.

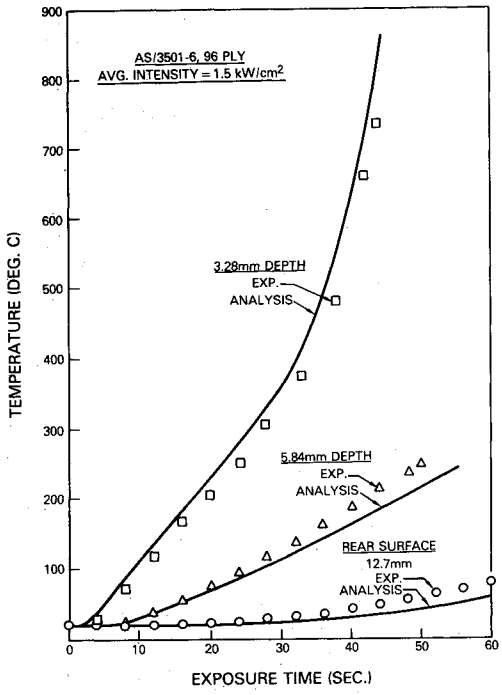

Fig. 4 Comparison of analytically derived and experimental temperature vs time response for 96-ply graphite epoxy.

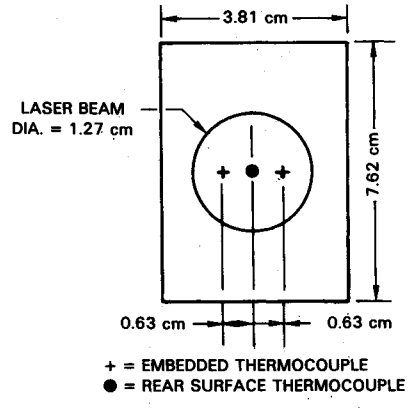

THERMAL TEST SPEC.

SPEC. THICKNESS (mm.)	STACKING SEQ.
3.18 (24 PLY)	$[\pm 45/0_2/\pm 45/0_2/\pm 45/0/90]_s$
6.35 (48 PLY)	$[\pm 45/0_2/\pm 45/0_2/\pm 45/0/90]_{2s}$
12.7 (96 PLY)	$[\pm 45/0_2/\pm 45/0_2/\pm 45/0/90]_{4s}$

Fig. 5 Geometry and stacking sequence of graphite epoxy thermal test specimens.

axisymmetric finite-difference model described previously. An average radial conductivity was established for each specimen thickness by first rotating the transverse and fiber direction conductivities for each ply into the longitudinal and width directions. The width direction conductivity for each ply was determined and the averaged value was then employed in the numerical calculations. To satisfy the boundary conditions in the width direction at the specimen mid-length, the specific thermal problem analyzed was that of a disk with a diameter equal to the specimen width W, which was assumed insulated around the circumference, $r = W/2$ (see Fig. 1, bottom). Examination of Figs. 3 and 4 indicates the agreement attained between the experimental and theoretical results, using the model presented and the derived thermophysical properties.

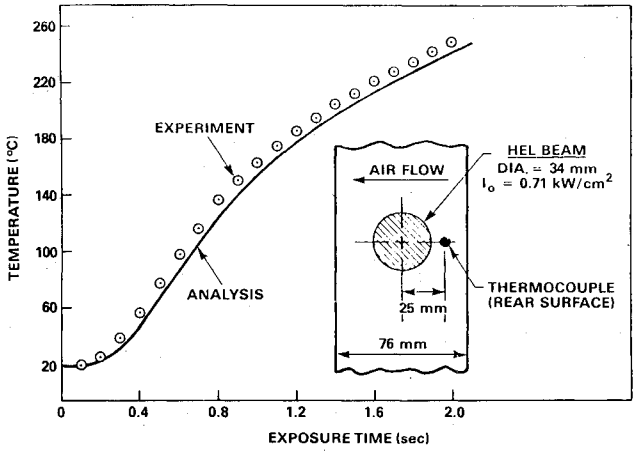

Fig. 6 Comparison of theoretical and experimental temperature vs time responses for 7075-T6 aluminum alloy.

Table 1 Constitutive law and equilibrium equations pertaining to thermomechanical response of isotropic materials[a]

Structural mechanics field equations

Duhamel-Neumann law:

$$\tau_{ij} = \lambda\theta\delta_{ij} + 2\mu e_{ij} - \alpha(3\lambda + 2\mu)T\delta_{ij} \quad (1)$$

Equation of equilibrium:

$$\tau_{ij,j} = F_i = \rho\ddot{u}_i \quad (2)$$

(1) and (2) governing PDE:

$$\mu\nabla^2 u_i + (\lambda+\mu)\theta_{,i} + F_i - \beta T = \rho\ddot{u}_i$$

Boundary conditions:

$$\bar{T}_i = \tau_{ij}\nu_j \qquad u_i = \bar{u}_i$$

Initial conditions:

$$u_i = U_i(X_i, 0)$$

[a] τ = stress; μ = shear modulus; λ = Lame constant; θ = expansion per unit volume; e = strain; α = thermal expansion coefficient; F = body force; u = displacement.

Figure 6 shows similar results for a 0.81-mm-thick 7075-T6 aluminum panel irradiated at a peak intensity of 0.71 kW/cm^2. The specimen geometry, beam diameter, and rear surface thermocouple location are illustrated in the inset drawing. Again, excellent agreement is evident between theoretical and experimental results. Material properties utilized in the model were taken from Refs. 7 and 8.

III. Stress and Fracture Analysis

The stress distribution in an isotropic, linear elastic solid subjected to combined thermal and mechanical loads is computed using the constitutive law and equilibrium equations given in Table 1. It should be noted that these field equations are directly coupled to the heat transfer equations given Sec. II in that the stress equations involve temperature-dependent mechanical properties and thermal stress effects, and their solution depends on the body geometry which may change due to ablation/melting phenomena.

Composite Structures

For composite structures, a stress analysis based on the finite-element method has been developed which incorporates the Mindlin laminated plate theory.[9] Deflections due to both

transverse shear and bending are included in the formulation. With respect to the x, y, and z coordinate system indicated in the right-hand side of Fig. 7, the displacement field for each element is given by

$$u(x,y,z,t) = u_o(x,y,t) - z\psi_x(x,y,t)$$

$$v(x,y,z,t) = v_o(x,y,t) - z\psi_x(x,y,t)$$

$$w(x,y,z,t) = w_o(x,y,t) \tag{8}$$

where u_o, v_o, and w_o are the midplane displacements in the x, y, and z directions, respectively, and ψ_x and ψ_y are rotations normal to the x-z and y-z planes, respectively. Using the classical definitions of strain in conjunction with Eq. (8), the strain tensor for the element is readily expressed in terms of the five plate displacement variables u_o, v_o, w_o, ψ_x, and ψ_y. For most fiber-reinforced laminated composites, each layer may be considered as an orthotropic material whose constitutive response is represented by

$$\begin{Bmatrix} \sigma_{xx} \\ \sigma_{yy} \\ \sigma_{xy} \\ \sigma_{yz} \\ \sigma_{xz} \end{Bmatrix} = \begin{bmatrix} \bar{Q}_{11} & \bar{Q}_{12} & \bar{Q}_{16} & 0 & 0 \\ \bar{Q}_{12} & \bar{Q}_{22} & \bar{Q}_{26} & 0 & 0 \\ \bar{Q}_{16} & \bar{Q}_{26} & \bar{Q}_{66} & 0 & 0 \\ 0 & 0 & 0 & \bar{Q}_{44} & \bar{Q}_{45} \\ 0 & 0 & 0 & \bar{Q}_{45} & \bar{Q}_{55} \end{bmatrix} \begin{Bmatrix} \epsilon_{xx} - \alpha_x \Delta T \\ \epsilon_{yy} - \alpha_y \Delta T \\ \gamma_{xy} - \alpha_{xy} \Delta T \\ \gamma_{yz} \\ \gamma_{xz} \end{Bmatrix} \tag{9}$$

where $\bar{Q}_{ij}(i,j=1,2,6)$ are the transformed in-plane stiffness components for a state of plane stress,[10] $\bar{Q}_{ij}(i,j=4,5)$ are the reduced transverse shear stiffnesses, ΔT is the temperature rise, and α_x, α_y, and α_{xy} are the transformed thermal expansion coefficients. Using Eq. (9) in conjunction with the strain-displacement relationship and the prescribed boundary conditions, the potential energy of the finite-element network is easily formulated. Minimization of this functional with respect to the nodal point displacements yields the following matrix equaillibrium equation:

$$[K]\{\delta\} = \{F^e\} + \{F^T\} \tag{10}$$

where $\{\delta\}$ refers to the overall system displacement vector, $[K]$ is the system stiffness matrix, and $\{F^e\}$ and $\{F^T\}$ represent the mechanical and thermal statically equivalent nodal point load vectors, respectively. The vectors $\{\delta\}$, $\{F^e\}$, and $\{F^T\}$ contain $5N$ terms, where N is the total number of nodal points; $[K]$ is a $5N \times 5N$ symmetric matrix.

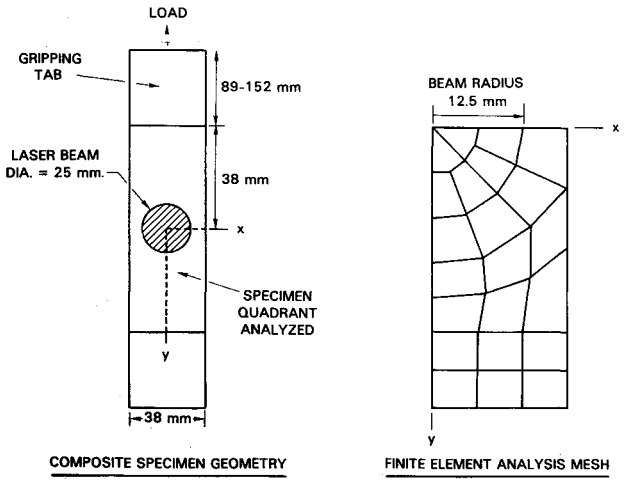

Fig. 7 Specimen geometry and corresponding finite-element model for irradiated tension panel.

A simple but effective approach for treating elevated-temperature failure of composites is a ply-by-ply analysis based on the maximum stress theory.[9,10] The maximum stress criterion states that lamina failure occurs when the stresses referred to the material axes exceed the prescribed critical temperature-dependent strengths. If σ_1, σ_2, and σ_{12} denote the longitudinal (fiber direction), transverse, and shear stresses with respect to the material directions, and X_t, X_c, Y_t, Y_c, and S denote the corresponding strengths (t and c refer to tension and compression, respectively), then the maximum stress criterion is expressed by

$$\begin{aligned} &\sigma_1 > X_t \qquad (\sigma_1 > 0) \\ &\sigma_1 < X_c \qquad (\sigma_1 < 0) \\ &\sigma_2 > Y_t \qquad (\sigma_2 > 0) \\ &\sigma_2 < Y_c \qquad (\sigma_2 < 0) \\ &|\sigma_{12}| > S \end{aligned} \tag{11}$$

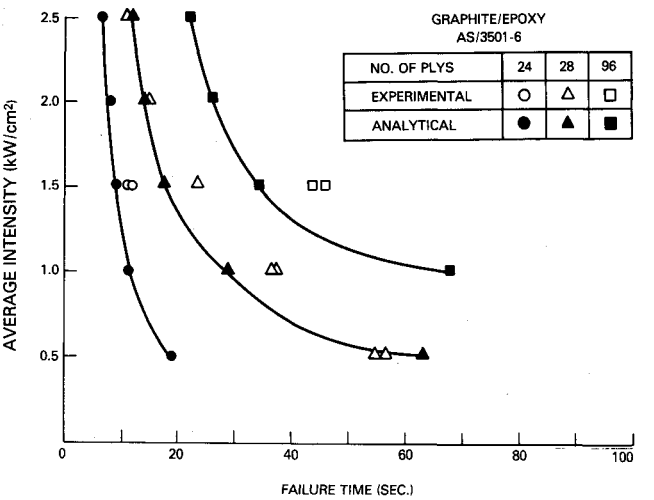

Fig. 8 Experimental and analytical relationships between heat intensity and failure time for spot-irradiated, graphite epoxy tension specimens.

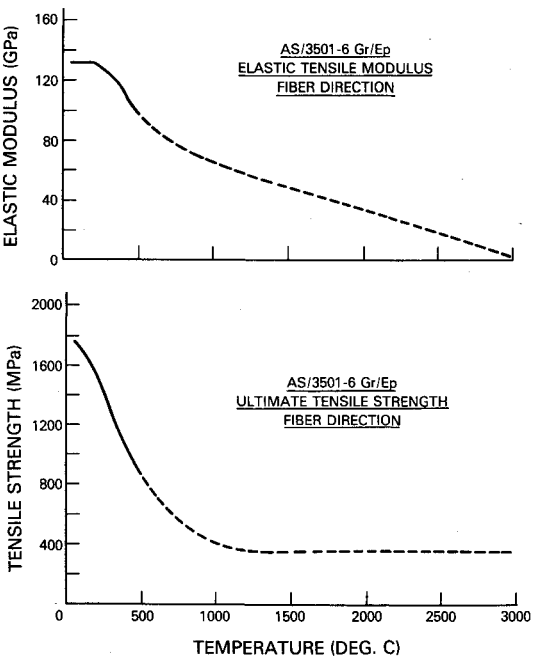

Fig. 9 Temperature dependence of the fiber direction tensile strength and modulus for graphite epoxy.

The first two conditions in Eq. (11) pertain to fiber failure, whereas the third and fourth conditions represent matrix failure. The last condition refers to in-plane shear fracture. In the finite-element analyses, fiber failure is implemented by setting the stiffnesses Q_{11}, Q_{12}, Q_{66}, and Q_{55}, equal to a very small value. For matrix failure, Q_{22}, Q_{12}, Q_{66} and Q_{44} are similarly assigned a near-zero value. In the event of a shear failure, Q_{66}, is equated to a small quantity.[9]

In using the stress and failure models to predict elevated-temperature structural response, the analysis is conducted incrementally with respect to the thermal results discussed in Sec. II. For each time increment mechanical properties are defined using the instantaneous temperature distribution and a finite-element solution is obtained [Eq. (10)]. Stresses in all plies are examined for failure according to Eq. (11). If failure is detected, the appropriate laminae stiffness are reduced. To account for the efforts of load redistribution as a result of local failure, solution of Eq. (10) is again repeated and each ply is again tested for failure. If additional fracture occurs, the process is repeated; if not, the solution proceeds to the next time step. The analysis continues until a stifficiently large number of elements have failed such that large, extensive global deflections occur, which implies a nearly singular overall stiffness matrix [K].

Figure 8 shows the experimental and analytically derived relationship between irradiation intensity and failure time for graphite epoxy tension specimens having 24, 48, and 96 plies. The stacking sequence of the material was identical to that given in Fig. 5, and the same 15 kW laser device described in Sec. II was utilized as a heat source. Figure 8 illustrates the overall specimen geometry and beam size, as well as the finite-element mesh used to model the spot-irradiated coupons. A preload equal to approximately 25% of the room temperature ultimate strength was applied to the test articles and maintained constant throughout the irradiation period. Owing to symmetry considerations, the analytical model incorporated only one quadrant of the specimen geometry and employed 9-noded isoparametric finite elements. The most important temperature-dependent mechanical properties which influence the computed failure response are the ultimate tensile strength and elastic modulus. These parameters are shown in Fig. 9 for the fiber direction, and in Fig. 10 for the transverse orientation. The solid portion of these curves represents actual data obtained from Greszczuk,[11] which were obtained after exposing the material at temperature for approximately 4 s. The extensive dashed portion of the fiber-direction properties vs temperature curves represent an extrapolation of data obtained below 500°C. The temperature dependence of other properties (e.g., compressive strengths, shear moduli, and coefficients of thermal expansion) was taken from Ref. 9.

As expected, Fig. 8 shows that the applied heating intensity varies inversely with failure time t_f for a given material thickness due to the more rapid ablation and material property degradation associated with the higher intensities. In addition, both the analytical and experimental results show that for a given intensity, longer exposure times are required for failure of thicker laminates due to the fact that more extensive through-thickness damage in the irradiated zone is required to elevate the stress to sufficiently high level for failure to initiate. The 48-ply curve indicates that the best agreement between analysis and experimental data occurs at the extreme intensity levels 0.5 and 2.5 kW/cm^2, where the computed failure times exceed the measured values by only 10 and 13%, respectively. At the intermediate intensities (1.0, 1.5, and 2.0 kW/cm^2), the calculated t_f values consistently underestimate the measured times by as much as 25%. However, in view of the uncertainty in mechanical properties and the simplified treatment of resin decomposition and ablation, the agreement between experiment and anlaysis is quite good.

Metallic Structures

Figure 11 indicates the experimental and theoretical relationship between applied load and failure time for 0.81-mm-thick 7075-T6 aluminum alloy. The 75-mm-wide specimens were laser-irradiated with beam diameters of 17.8, 34.0, and 55.9 mm. Note that the failure loads are normalized with respect to the room temperature ultimate strength. To establish the intrinsic strength of this alloy under rapid heating conditions, a supplementary series of tests were conducted in which 25.4-mm-wide coupons were flood-irradiated over the entire width while subjected to various fractions of their room temperature strength. After recording the failure temperature associated with each load level, the relationship between short-time (0.02–0.5 s fracture time) ultimate strength and temperature was established as shown by the data points in Fig. 12. The solid curve in this figure shows the conventional relationship obtained by preheating the material for 30 min prior to testing. The pronounced decrease in strength with

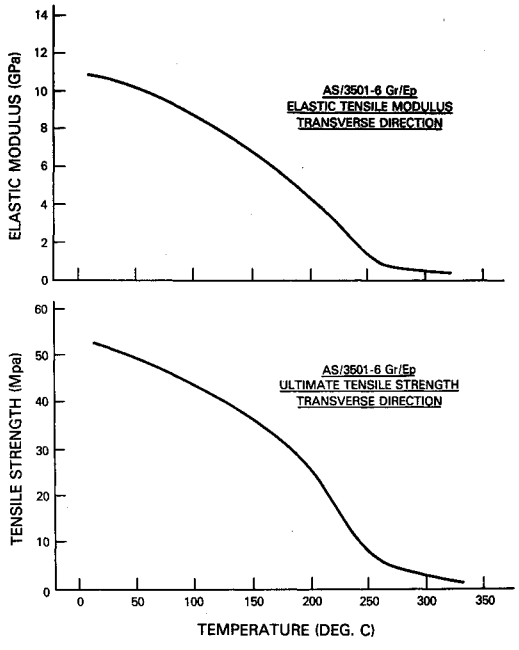

Fig. 10 Temperature dependence of the transverse strength and modulus for graphite epoxy.

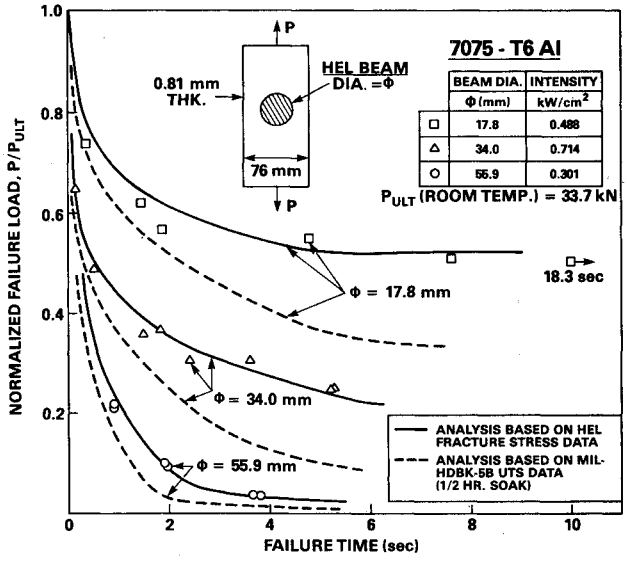

Fig. 11 Theoretical and experimental relationship between applied load and failure time for 0.81 mm-thick 7075-T6 aluminum alloy.

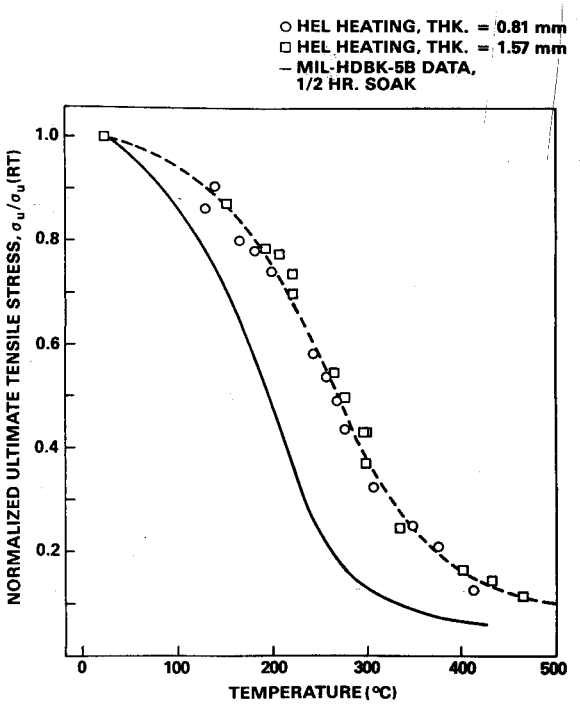

Fig. 12 Ultimate strength vs temperature for 7075-T6 aluminum as determined both under rapid heating and after a 30 min pre-soak.

temperature exhibited at both heating rates is due largely to accelerated overaging and annealing reactions which occur in this precipitation hardening alloy. The less abrupt strength reduction for the rapidly (laser) heated material reflects the fact that shorter times at temperature are available for these diffusion-controlled reactions to occur.

In generating the theoretical curves shown in Fig. 11, the lumped-mass thermal analysis described in Sec. II was adopted, and the necessary thermophysical properties were taken from Refs. 7 and 8. The corresponding stress/failure analysis was essentially a limit analysis in which it is assumed that at complete panel collapse, each point on the cross section simultaneously attains its temperature-dependent fracture stress. To predict the failure load P_f corresponding to an exposure time t_f, the temperature distribution across the panel width is computed, and then by employing the fracture strength vs temperature relationships (Fig. 12), the stress distribution at failure over the cross section is defined. Integration of this stress profile then provides the ultimate panel load at t_f. Explicitly, the fracture load is computed according to

$$P_f = \int_0^b \int_0^w \sigma_u[T(r,z,t_f)]\,dr\,dz \qquad (12)$$

where b represents the panel thickness, w denotes the specimen width, $\sigma_u(T)$ is the measured dependence of fracture stress on temperature, and $T(r,z,t_f)$ denotes the computed spatial temperature distribution at time t_f. The coordinates r and z are shown in Fig. 1. It should be noted that Eq. (12) is approximate in that creep and thermal stress effects are not considered. Futhermore, the assumed stress state at failure does not necessarily satisfy the material's constitutive law and the equilibrium field equations.

Examination of Fig. 11 shows that for each beam diameter an initial rapid drop in fracture load with increasing exposure time is apparent, which is due to reduction in cross section produced by burnthrough of the panel. As expected, this effect is most severe for the larger diameter beams. The more modest reduction in failure load at longer exposure times ($t_f > 2$ s) is caused primarily by the fact that heat conduction into the unirradiated flanks of the panel is required to induce sufficient thermal degradation in fracture stress to cause collapse. Analytical results are shown in Fig. 11 using both the rapid-heating (0.02–0.5 s) and long-time (30 min-soak) strength vs temperature data. Examination of the solid curves reveals that use of the high-heating-rate strength data results in excellent agreement with the experiments, whereas incorporation of the 30 min-soak properties into the analysis (dashed curves) leads to significant underestimation of the failure load often by as much as 50%.

IV. Summary of Results

The primary conclusions resulting from the present investigation regarding prediction of the survivablility of structures exposed to a severe thermal environment are as follows:

1) A detailed description of both one- and two-dimensional thermal analyses of the response of metallic and composite materials to intense heating has been presented. These models include nonlinear effects such as temperature-dependent maerial properties, re-irradiation surface losses, and melting/ablation phenomena. Experimental transient temperature data obtained on both 7075-T6 aluminum and AS/3501-6 graphite epoxy laminates show excellent agreement with theoretical projections. It should be noted that for organic-matrix composite materials, the present formulation addresses the complex, time-dependent, resin decomposition reactions by inclusion of these effects into the heat capacity vs temperature relationship. If necessary, it may be possible to improve the present model by including one or more Arrhenius kinetic expressions into Eqs. (1) and (7).

2) For composite materials subjected to combined mechanical and severe thermal loads, a flat-plate laminate finite-element model based on the Mindlin theory has been formulated. A procedure for applying this code together with a maximum stress failure criterion to predict failure initiation and subsequent unstable growth (collapse) has also been outlined. Good agreement between theoretical and experimentally determined failure times has been shown for laminated graphite epoxy tension coupons spot-irradiated at intensities in the range 0.5–2.5 kW/cm^2.

3) The present study has demonstrated that in assessing the elevated-temperature mechanical response of metallic structures, it is important that both temperature and heating rate be considered in defining the intrinsic ultimate tensile strength of the material. For example, at any given temperature, it has been shown that for 7075-T6 aluminum the short-time (0.02–0.5 s fracture time) tensile strength is significantly greater than that obtained by pre-heating the material for 30 min prior to test. The limit analysis that was employed to predict the fracture time for spot-irradiated panels subjected to a wide range of applied loads and beam diameters provided excellent correlation with experimental data. More accurate analytical results may be anticipated if a finite-element analysis using a thermoelastoplastic-creep model were adopted.

References

[1]Pering, G. A., Farrell, P. V., and Springer, G. S., "Degradation of Tensile and Shear Properties of Composite Exposed to Fire or High Temperature," *Journal of Composite Materials*, Vol. 14, Jan. 1980, p. 54–68.

[2]Kibler, K. G., Carter, H. G., and Eisenmann, J. R., "Response of Graphite Composites to Laser Irradiation," Air Force Office of Scientific Research, Bolling AFB, Washington, DC, TR-77-0706, March 1977.

[3]Kibler, K. G., Carter, H. G., and Eisenmann, J. R., "Residual Strength of Laser-Damaged Graphite Composites," *Journal of Composite Materials*, Vol. 9, Jan. 1975, p. 28–32.

[4]Griffis, C. A., Masumura, R. A., and Chang, C. I., "Thermal Response of Graphite Epoxy Composite Subjected to Rapid Heating," *Journal of Composite Materials*, Vol. 15, Sept. 1981, p. 427–442.

[5]Griffis, C. A., Chang, C. I., and Stonesifer, F. R., "Thermo-Mechanical Response of Tension Panels Under Intense Rapid Heating," *Theoretical and Applied Fracture Mechanics*, Vol. 3, April 1985, pp. 41–48.

[6]Menousek, J. F. and Monin, D. L., "Laser Thermal Modeling of Graphite Epoxy," Naval Weapons Center, China Lake, CA, Tech. Memo. Rept. 3834, June 1979.

[7]*Aerospace Structural Metals Handbook, Vol. II (Non-Ferrous Alloys)*, Mechanical Properties Data Center, Stulen Inc., Traverse City, MI, Tech. Rept. AFML-TR-68-115, 1973.

[8]*Metals Handbook*, American Society for Metals, Cleveland, OH, 1948.

[9]Sun, C. T., Chen, J. K., and Chang, C. I., "Failure of a Graphite/Epoxy Laminate Subjected to Combined Thermal and Mechanical Loading," *Journal of Composite Materials*, Vol. 19, Sept. 1985, p. 408–423.

[10]Jones, R. M., *Mechanics of Composite Materials*, Technomic, Westport, CT, 1980.

[11]Under Rapid Heating," Final Report, N00014-83-C-2330, Naval Research Laboratory, Washington, DC, Contract N00014-83-C-2330, Dec. 1984.